



Available online at www.sciencedirect.com

SciVerse ScienceDirect

Acta Materialia 61 (2013) 5743–5755



www.elsevier.com/locate/actamat

The influences of temperature and microstructure on the tensile properties of a CoCrFeMnNi high-entropy alloy

F. Otto^{a,b,*}, A. Dlouhý^c, Ch. Somsen^d, H. Bei^a, G. Eggeler^d, E.P. George^{a,b}

^a Materials Science and Technology Division, Oak Ridge National Laboratory, Oak Ridge, TN 37831, USA

^b Materials Science and Engineering Department, University of Tennessee, Knoxville, TN 37996, USA

^c Institute of Physics of Materials, Academy of Sciences of the Czech Republic, 616 62 Brno, Czech Republic

^d Institut fuer Werkstoffe, Ruhr-Universitaet Bochum, 44780 Bochum, Germany

Received 23 March 2013; received in revised form 11 June 2013; accepted 12 June 2013

Available online 28 June 2013

Abstract

An equiatomic CoCrFeMnNi high-entropy alloy, which crystallizes in the face-centered cubic (fcc) crystal structure, was produced by arc melting and drop casting. The drop-cast ingots were homogenized, cold rolled and recrystallized to obtain single-phase microstructures with three different grain sizes in the range 4–160 µm. Quasi-static tensile tests at an engineering strain rate of 10^{-3} s⁻¹ were then performed at temperatures between 77 and 1073 K. Yield strength, ultimate tensile strength and elongation to fracture all increased with decreasing temperature. During the initial stages of plasticity (up to ~2% strain), deformation occurs by planar dislocation glide on the normal fcc slip system, {111}{110}, at all the temperatures and grain sizes investigated. Undissociated 1/2{110} dislocations were observed, as were numerous stacking faults, which imply the dissociation of several of these dislocations into 1/6{112} Shockley partials. At later stages (~20% strain), nanoscale deformation twins were observed after interrupted tests at 77 K, but not in specimens tested at room temperature, where plasticity occurred exclusively by the aforementioned dislocations which organized into cells. Deformation twinning, by continually introducing new interfaces and decreasing the mean free path of dislocations during tensile testing (“dynamic Hall-Petch”), produces a high degree of work hardening and a significant increase in the ultimate tensile strength. This increased work hardening prevents the early onset of necking instability and is a reason for the enhanced ductility observed at 77 K. A second reason is that twinning can provide an additional deformation mode to accommodate plasticity. However, twinning cannot explain the increase in yield strength with decreasing temperature in our high-entropy alloy since it was not observed in the early stages of plastic deformation. Since strong temperature dependencies of yield strength are also seen in binary fcc solid solution alloys, it may be an inherent solute effect, which needs further study.

© 2013 Acta Materialia Inc. Published by Elsevier Ltd. All rights reserved.

Keywords: High-entropy alloys; Mechanical properties; Deformation twinning; Yield strength; Temperature dependence

1. Introduction

Solid solution alloys consisting of multiple principal elements in approximately equiatomic concentrations have been the subject of a rapidly increasing body of research since Yeh et al. [1] defined this new class of metallic alloys,

now commonly referred to as high-entropy alloys. A solid solution alloy consisting of five or more elements in equiatomic proportions is intriguing because of its potential for solid solution hardening (high strength) combined with good ductility if the solid solution phase possesses a simple crystal structure, e.g. face-centered cubic (fcc), with a large number of slip systems. Since high strength and ductility are important for structural materials, research efforts have tended to be application driven and directed towards finding new alloy compositions with promising mechanical properties. Numerous equiatomic multi-component alloys

* Corresponding author at: Materials Science and Technology Division, Oak Ridge National Laboratory, Oak Ridge, TN 37831, USA. Tel.: +1 865 574 6917; fax: +1 865 576 6298.

E-mail address: frederik.otto@rub.de (F. Otto).

have been reported in the literature and some mechanical properties have been assessed with mixed results (e.g. [2–12]). Despite this considerable effort, little is known concerning the basic deformation mechanisms in this class of alloys due to the following main reasons.

Most of the equiatomic alloys described in the literature do not consist of a single solid solution phase; instead, they contain multiple phases, including secondary solid solution phases and/or intermetallic compounds [6–10]. Thus, the measured mechanical properties, all obtained in compression, represent composite responses of the multiphase microstructures. This might be sufficient for a rough screening of candidates with promising mechanical properties, but it is difficult to develop a fundamental understanding based on such studies, e.g. the extent and mechanisms of solution hardening in high-entropy alloys. Additionally, interesting aspects of their basic mechanical properties might be obscured by the presence of secondary phases.

In a few cases where single-phase solid solution alloys were successfully produced and mechanically tested [11,12], no efforts were made to break down the cast microstructure by thermomechanical treatment. This may be partially due to the fact that these alloys consisted of refractory metals with high melting points which are brittle at low homologous temperatures and therefore difficult to process [11,12]. Regardless, the measured compressive mechanical properties were influenced by the coarse, heterogeneous grain structure and chemical gradients (segregation) in the microstructure as a result of the dendritic solidification during casting.

There have been two studies of rolled and recrystallized single-phase high-entropy alloys: one in which room-temperature hardness was investigated as a function of grain size [13] and the other in which preliminary tensile tests were performed at different temperatures [14]. However, there have been no efforts to investigate the nature of dislocations that operate in these alloys. If atoms are randomly distributed in a solid solution high-entropy alloy, the atomic environment around dislocations varies constantly as they move through the material. For an interpretation of the mechanical properties of high-entropy alloys, it is therefore mandatory to study dislocation plasticity in more detail.

In the present study, we address these shortcomings by investigating an equiatomic five-element CoCrFeMnNi alloy that was first reported by Cantor et al. [15]. It has been shown that this alloy consists of a single fcc solid solution phase exhibiting a high degree of thermodynamic stability [16] and excellent malleability [14]. Processing to break down the cast structure is possible by conventional methods such as rolling followed by recovery and recrystallization [13,14]. Gali and George [14] conducted an initial assessment of the tensile properties of the alloy being investigated here, as well as a related medium-entropy alloy, CoCrFeNi, both of which they thermomechanically processed by hot rolling.

Our goal here was to perform a detailed study of the mechanical properties of the CoCrFeMnNi high-entropy

alloy with special focus on the influence of temperature and microstructure. We present results from quasi-static tensile tests for three different grain sizes (4.4, 50 and 155 μm) and test temperatures between 77 and 1073 K. Wherever possible, the mechanical properties are related to the deformation mechanisms uncovered by transmission electron microscopy (TEM).

2. Material and methods

2.1. Experimental methods

Rectangular ingots ($127 \times 25.4 \times 12.7 \text{ mm}^3$) of the equiatomic CoCrFeMnNi alloy weighing $\sim 475 \text{ g}$ were produced by arc melting and drop casting under pure Ar atmosphere. The purity of each of the raw materials was at least 99.9%. Since Mn rapidly oxidizes in air, the Mn stock was cleaned in an aqueous solution of nitric acid immediately before it was added to the other materials in the arc melter. Additionally, because Mn has a high vapor pressure [17], it was stacked between the other constituents to minimize evaporation. Nevertheless, we found that there was weight loss during arc melting and an additional gram of Mn had to be added per ingot to compensate for its evaporation. After the raw materials were loaded in the arc melter, the chamber was first evacuated to $\sim 7 \times 10^{-4} \text{ Pa}$ and then backfilled with Ar gas to a pressure of $\sim 8.4 \times 10^4 \text{ Pa}$. Before the high-entropy alloy was melted, a small piece of Zr was melted to getter any residual oxygen that might be present in the chamber. The arc-melted buttons were flipped and remelted five times to promote homogeneity and thorough mixing of the elements before they were dropped into the rectangular Cu mold.

The drop-cast ingots were cleaned in an aqueous solution of hydrochloric acid and hydrogen peroxide, encapsulated in evacuated quartz ampules and solution-annealed for 48 h at 1473 K. The ingots were subsequently cold rolled along the longitudinal ingot direction to sheets having a final thickness of $\sim 1.7 \text{ mm}$. Starting from their initial thickness of 12.7 mm, this corresponds to a reduction in thickness of $\sim 87\%$. A few cross-rolling steps were introduced in between to increase the width of the rolled sheets to approximately 40 mm. The rolled sheets were annealed for 1 h at 1073, 1273 or 1423 K to obtain fully recrystallized microstructures with three different grain sizes. The 1423 K anneal was conducted in an evacuated quartz capsule; the other two anneals were conducted in air resulting in only minor surface oxidation.

Flat dog-bone-shaped tensile specimens with a gauge length of 12.7 mm were machined from the recrystallized sheets by electric discharge machining with their longitudinal axes perpendicular to the rolling direction of the sheet. The tensile specimens were ground carefully on each side with SiC paper, resulting in a final specimen thickness of 1.6 mm and a gauge section width of 3.14 mm. Vickers microhardness indents (300 g load) were made at the ends of the gauge section to enable the measurement of strain

by means of an optical traveling microscope. Tensile tests were performed at an engineering strain rate of 10^{-3} s^{-1} in a screw-driven Instron 4204 test rig. Two tests were performed for each material state at temperatures of 77, 293, 473, 673, 873 and 1073 K. Tests at room temperature and above were conducted in air. For tests at 77 K, the specimen and grips were immersed in a liquid nitrogen bath for about 10–15 min before the start of the test and stayed completely submerged during the test. For all temperatures above room temperature, the sample was brought to temperature by radiative/convective heat transfer from an induction-heated stainless steel susceptor. Once the desired test temperature was reached, the sample was held there for 15–30 min before the start of the test.

To investigate the evolution of microstructure with accumulated strain, additional tensile specimens were deformed at test temperatures of 77, 293 and 873 K, and the tests were interrupted at various strain levels. Thin sheets with a thickness of about 300 μm were carefully extracted from their gauge sections by electric discharge machining and ground down to foils having a thickness of about 100–120 μm using fine SiC paper. Discs with a diameter of 3 mm were punched out of the foils and electron transparent regions were produced in a twin jet polishing system using an aqueous electrolyte containing 21% acetic acid at a temperature of 15 °C and an applied voltage of 20 V. TEM investigations were conducted in an FEI Tecnai G2 SuperTwin and a Philips CM20 microscope operated at 200 kV. Scanning electron microscopy investigations were conducted in a JEOL 6500F microscope equipped with a field emission gun operated at 15 kV.

3. Results

3.1. Initial microstructures

Figs. 1 and 2 show the microstructures of CoCrFeMnNi sheets after cold rolling and annealing. The backscattered electron micrographs of Fig. 1, taken along the three principal sheet directions, RD (rolling direction), ND (normal

direction) and TD (transverse direction), clearly reveal homogeneous equiaxed grain structures. In the recrystallized state, many of the grains are found to contain annealing twins. The average grain sizes determined by a linear intercept method were found to be 4.4, 50 and 155 μm for annealing temperatures of 1073, 1273 and 1423 K (twin boundaries were not counted in the measurements). These materials will be referred to as FG (fine-grained), MG (medium-grained) and CG (coarse-grained) from now on. Grain size measurements on planes perpendicular to RD, ND and TD yielded almost identical values, confirming that the grains are indeed equiaxed after the three anneals. The representative TEM bright-field (BF) micrographs of Fig. 2 provide evidence that the grains in all three starting states are largely dislocation-free before the tensile tests. Figs. 1 and 2 also document the single-phase character of the alloy in accordance with what has been reported earlier [14,15].

3.2. Tensile properties

Fig. 3 shows representative engineering stress–strain curves for the FG (Fig. 3a) and CG (Fig. 3b) materials at the six test temperatures. The engineering strain in these curves is the ratio of cross-head displacement to the initial specimen gauge length (12.7 mm). The highest values of yield strength, ultimate tensile strength and elongation to fracture are all obtained at liquid nitrogen temperature (77 K). An increase in temperature results in a monotonic decrease in both the yield and ultimate tensile strengths. The same is true for the elongations to fracture of MG and CG; however, for FG (Fig. 3a), a minimum in ductility occurs in the intermediate temperature range, around 673 K. In this temperature range, pronounced serrations are present on the stress–strain curves for all three grain sizes; they extend from the yield point all the way up to where plastic instabilities develop and necking starts. Although it is difficult to discern in Fig. 3a, the stress–strain curves of the FG material exhibit clearly defined yield points in the temperature range between 77 and

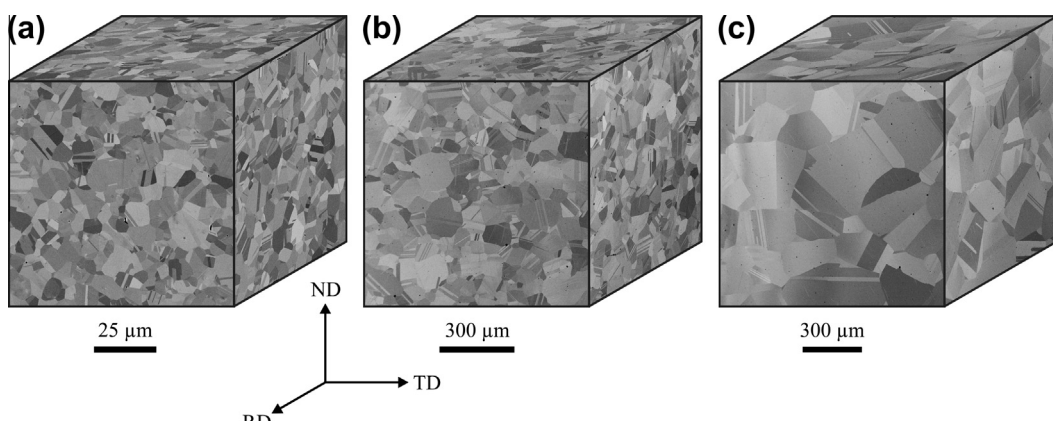


Fig. 1. Backscattered electron images of the microstructures of the CoCrFeMnNi alloy sheets after cold rolling (87% thickness reduction) and subsequent 1 h anneals at: (a) 1073 K, grain size 4.4 μm ; (b) 1273 K, grain size 50 μm ; and (c) 1423 K, grain size 155 μm .

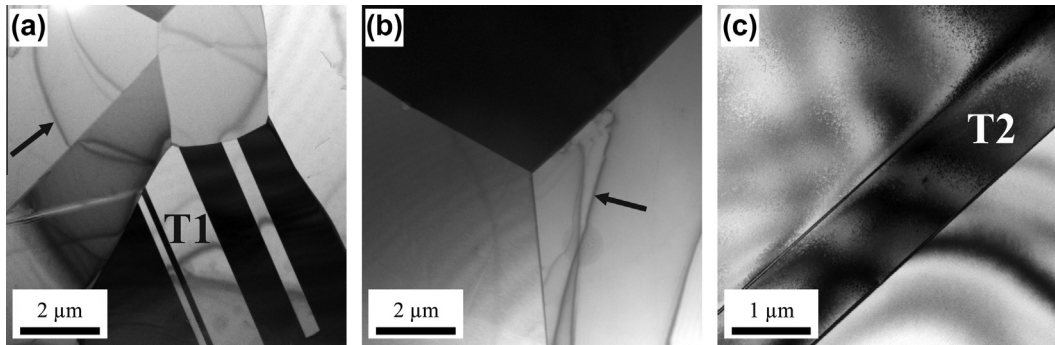


Fig. 2. TEM BF images of the microstructures of the CoCrFeMnNi sheets after cold rolling (87% thickness reduction) and 1 h anneals at: (a) 1073 K, grain size 4.4 μm ; (b) 1273 K, grain size 50 μm ; and (c) 1423 K, grain size 155 μm . Annealing twins are visible (labeled T1 and T2), as are bend contours (arrows). The grains are largely dislocation-free.

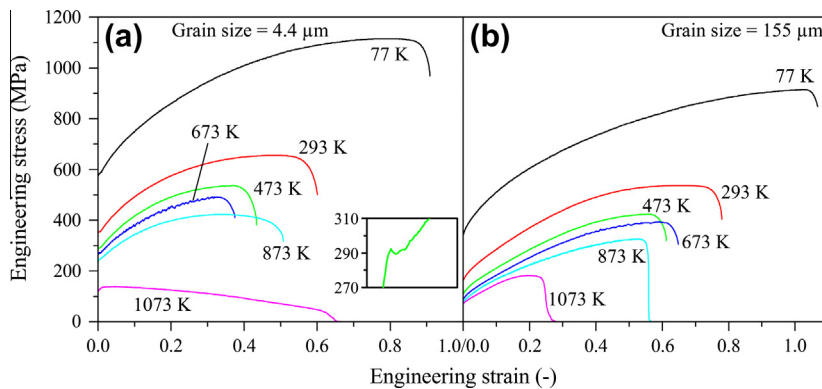


Fig. 3. Representative engineering stress–strain curves of the CoCrFeMnNi alloy at the six testing temperatures for the (a) fine-grained (grain size 4.4 μm) and (b) coarse-grained (grain size 155 μm) materials. The inset in (a) shows a small load drop after yielding for a fine-grained sample that was tested at 473 K.

473 K, but not at higher temperatures. An example is shown in the inset in Fig. 3a, which shows the region around the yield point for the FG material deformed at 473 K where a sharp yield point followed by a small load drop is observed. At 293 and 473 K, small load drops after yielding were observed in three out of four tests (two tests at each temperature and grain size). These yield-point phenomena are unique to the FG material; the stress–strain curves of MG and CG show neither well-defined yield points nor load drops after yielding. Another striking feature of Fig. 3a is that the FG sample tested at 1073 K reaches its maximum tensile strength relatively quickly (after only a few percent strain), although the sample does not fail until much later, at an engineering strain of more than 60%. This behavior is only observed for the FG material tested at 1073 K; tests performed at either lower temperatures or on materials with coarser grains usually exhibit failure shortly after the maximum tensile stress is reached (Fig. 3b).

Fig. 4 summarizes the temperature and grain size dependencies of the 0.2% offset yield strength σ_y (Fig. 4a and b), ultimate tensile strength σ_u (Fig. 4c) and elongation to fracture ε_f (Fig. 4d). Both the strengths and the ductility show strong temperature dependencies, with their maxima

occurring at liquid nitrogen temperature. For all three grain sizes, σ_y and σ_u decrease monotonically with increasing temperature (see Fig. 4a and c). The absolute changes in σ_y and σ_u are, however, most significant between 77 K and room temperature, where, in the extreme case of the CG material, the yield strength is halved and the tensile strength is reduced by more than 40% with increasing temperature.

At all temperatures up to 873 K, a strong increase in σ_y is observed upon refining the grain size from 155 down to 4.4 μm ; at 873 K, the yield strength of the CG material is about one third that of the FG material. However, the strength difference between the MG and CG materials (grain sizes of 50 and 155 μm) is small. Upon further increasing the test temperature from 873 to 1073 K, the MG and CG materials do not show any significant decrease in the yield strength while a substantial drop of almost 50% is observed for the FG material. Concomitantly, the ultimate tensile strength of the FG material drops below that of the MG and CG materials for the first time. To quantify the grain size dependence of yield strength, it is plotted in Fig. 4b following the well-known Hall–Petch relationship $\sigma_y = \sigma_0 + k \cdot d^{-1/2}$. The intercepts (σ_0) and slopes (k), obtained from linear fits of the data

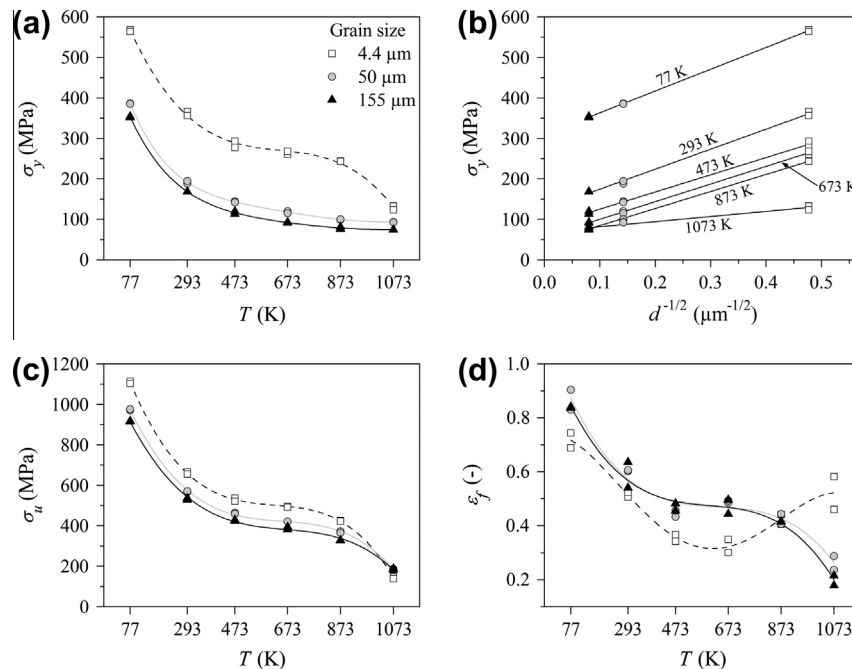


Fig. 4. Temperature and grain size dependence of (a, b) 0.2% offset yield stress (σ_y), (c) ultimate tensile strength (σ_u) and (d) elongation to fracture (ε_f) for the CoCrFeMnNi alloy.

in Fig. 4b, are compiled in Table 1 for the various test temperatures.

Differences between the FG material and the two materials with coarser grain sizes are also manifested in their elongations to fracture, ε_f , as depicted in Fig. 4d. In these curves, the elongation to fracture was determined by measuring, with a traveling microscope, the distances between the hardness indents at the ends of the gauge section and the corresponding fracture surfaces. Over the investigated temperature range, ε_f is virtually identical for the MG and CG materials. After a steep drop in ductility from 77 K to room temperature, there is a short plateau-like region at intermediate temperatures (473–673 K), after which ε_f drops again significantly. In contrast, the $\varepsilon_f(T)$ curve of the FG material exhibits a minimum at intermediate temperatures.

Fig. 5 shows the extent of work hardening, defined here as the difference between the ultimate and yield strengths, for the three grain sizes as a function of temperature. The curves are almost identical for the MG and CG materials in contrast to the FG material which exhibits a lower degree of work hardening generally. Qualitatively, the temperature dependence of work hardening is similar for the

three grain sizes, with the highest extent of work hardening observed at 77 K. No work hardening is observed at the highest test temperature for the FG material, which can also be seen in its stress-strain curve (Fig. 3a). Overall, the work hardening capability of the CoCrFeMnNi alloy decreases with increasing temperature for all three grain sizes and is lowest for the smallest grain size at room temperature and above.

3.3. Microstructural changes resulting from tensile deformation

Fig. 6a is a montage of TEM BF micrographs showing the typical dislocation structure in the CG material after a tensile strain of 1.7% at a test temperature of 873 K. The $\mathbf{g} = (11\bar{1})$ vector and the crystallographic orientation of the investigated grain with respect to the primary electron

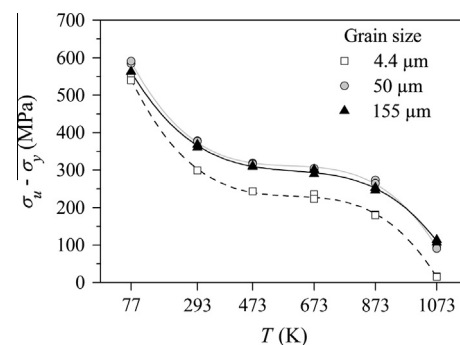


Fig. 5. Temperature and grain size dependence of the degree of work hardening in the CoCrFeMnNi alloy (defined here as the difference between the ultimate and yield strengths, $\sigma_u - \sigma_y$).

Table 1
Values of the Hall-Petch intercepts σ_0 and slopes k obtained from Fig. 4b.

T (K)	σ_0 (MPa)	k (MPa $\times \mu\text{m}^{-1/2}$)
77	310	538
293	125	494
473	83	425
673	57	436
873	43	421
1073	69	127

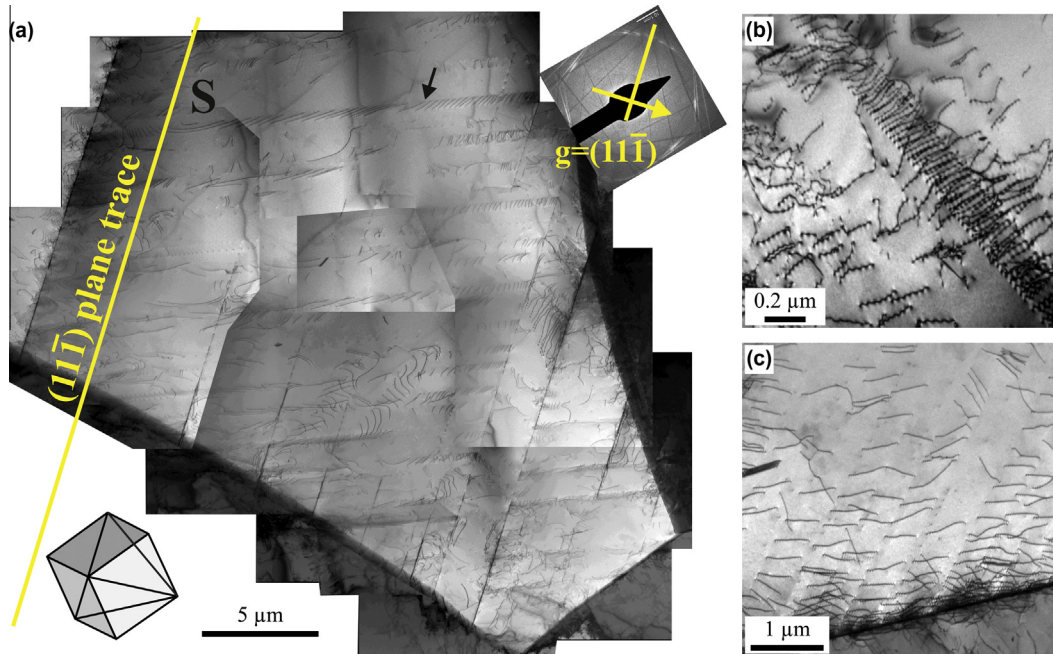


Fig. 6. Representative TEM BF micrographs from the gauge sections of interrupted tensile test specimens of the coarse-grained CoCrFeMnNi alloy (grain size 155 μm) after relatively small tensile strains: (a) 1.7% at 873 K, (b) 2.4% at 77 K and (c) 2.1% at 293 K. Planar slip of $1/2\langle 110 \rangle$ -type dislocations on $\{111\}$ -type fcc planes is a dominant feature at all three investigated temperatures.

beam \mathbf{B} (\mathbf{B} is 7° off the crystallographic direction [1 1 2]) are shown in the inset diffraction pattern. Further clarification of the image orientation is provided next to the BF montage in the form of a projection of an elementary fcc lattice cell onto the plane of the figure [18]. Fig. 6a clearly shows that, in the early stages of plastic deformation of the CoCrFeMnNi alloy, dislocation glide is strongly localized on a distinct set of $\{111\}$ -type fcc lattice planes. In the activated planes, dislocations form extended pile-ups against grain boundaries. One of the double-ended pile-ups in the $(\bar{1}\bar{1}\bar{1})$ plane is highlighted by a black arrow. The positive part of this pile-up, which is located on the right-hand side of the dislocation source denoted "S", contains more than 40 individual dislocations despite the applied stress having been removed upon unloading. The stability of the pile-up in the unloaded condition indicates the presence of a significant friction stress and resistance of the grain boundary to dislocation transmission/absorption. Planar $\{111\}$ dislocation slip dominates the early stages of deformation in the CG material not only at 873 K but also at lower deformation temperatures, as shown in Fig. 6b for a sample strained to 2.4% at 77 K and in Fig. 6c for a sample strained to 2.1% at 293 K.

In order to characterize the Burgers vectors of the dislocations discussed above, extensive tilting experiments were performed for the three temperatures and strain states depicted in Fig. 6. Burgers vector analysis based on the $\mathbf{g} \cdot \mathbf{b} = 0$ technique was employed where up to nine different, linearly independent \mathbf{g} vectors were analyzed per sample and images of the same area were taken under the corresponding two-beam diffraction conditions. Dislocations

for the analysis were randomly chosen in the investigated area until at least 10 cases were identified for which the TEM dislocation contrast vanished under two or more different \mathbf{g} conditions. The analyses yielded identical results for all three deformed conditions and only Burgers vectors of the type $1/2\langle 110 \rangle$ were identified. We can thus conclude that, in a broad temperature range (77–873 K), the early stages of plastic deformation in the CoCrFeMnNi high-entropy alloy are governed by the planar slip of $1/2\langle 110 \rangle$ -type dislocations on $\{111\}$ -type planes, which is in agreement with elementary dislocation processes observed earlier in concentrated binary fcc solid solutions (e.g. [19,20]).

Besides the complete $1/2\langle 110 \rangle$ -type dislocations, other interesting features were also detected in the deformed CG material. As shown in the TEM $\mathbf{g}/3\mathbf{g}$ weak-beam dark-field (WBDF) and BF micrographs of Fig. 7, stacking faults (SFs) were frequently observed after small plastic deformations. The SFs are marked by red arrows in Fig. 7a (2.4% strain at 77 K), Fig. 7b (2.1% strain at 293 K) and Fig. 7c (1.7% strain at 873 K). Although not unambiguously identified here, we expect partial dislocations, presumably of the Shockley $1/6\langle 112 \rangle$ -type, to bracket the SF ribbons, as in other fcc metals/alloys (e.g. [21]).

Another important feature of the investigated dislocation structures, which also formed during the early stages of deformation at temperatures to 873 K, is shown in the BF TEM micrographs of Fig. 8. Here, two planar dislocation groups that move in opposite directions on closely spaced $\{111\}$ planes have been arrested due to the attractive forces acting among the individual dislocations of the

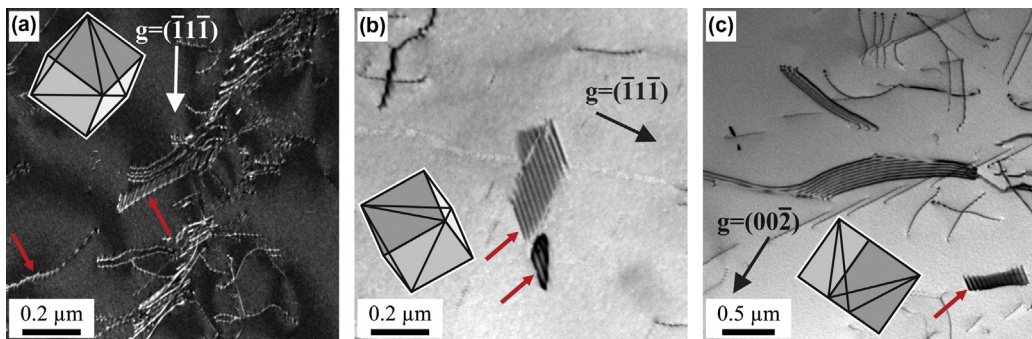


Fig. 7. Stacking faults (marked by red arrows) in the coarse-grained CoCrFeMnNi alloy (grain size 155 μm) after plastic deformations of (a) 2.4% at 77 K (WBDF), (b) 2.1% at 293 K (BF) and (c) 1.7% at 873 K (BF). (For interpretation to colors in this figure, the reader is referred to the web version of this paper.)

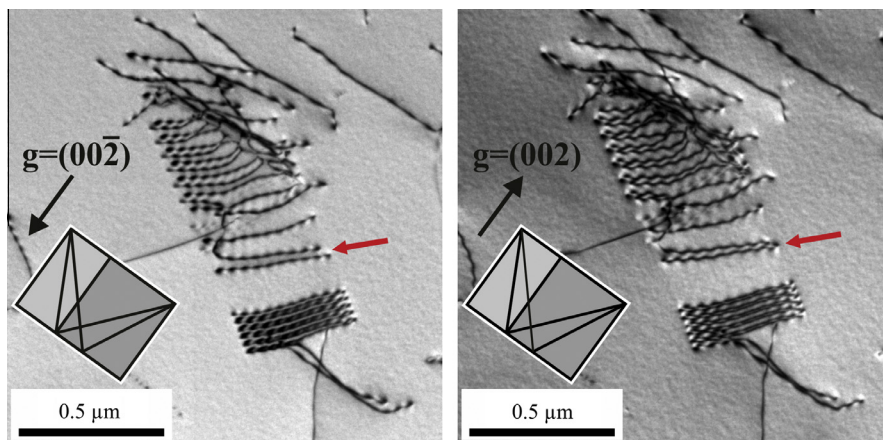


Fig. 8. Dislocation multipole in the coarse-grained CoCrFeMnNi alloy (grain size 155 μm) after plastic deformation of 1.7% at 873 K. The two BF images were acquired using reverse g vectors in order to demonstrate that the individual dislocation pairs are dipoles. (For interpretation to colors in this figure, the reader is referred to the web version of this paper.)

positive group (Burgers vector $+b$) and the negative group (Burgers vector $-b$). The multipole character of this dislocation arrangement is illustrated in Fig. 8 by reversing the sense of the operating diffraction vector g . When the g -condition changes from $-g$ (Fig. 8a) to $+g$ (Fig. 8b), the separation between corresponding dislocation counterparts changes in agreement with the rules governing the relative positions of the dislocation core and its diffraction contrast image [22,23]. As an example, one of the elementary dipoles that obeys this contrast rule is highlighted by a red arrow in Fig. 8a and b.

In contrast to the initial stages of deformation (up to plastic strains of 2.4%), distinct microstructural differences can be observed at higher strains. The TEM and high-resolution TEM images shown in Fig. 9 reveal extensive deformation twinning in the FG specimen deformed to a plastic strain of 20.2% at 77 K. A lower magnification overview of the twinned microstructure is presented in Fig. 9a. This scanning transmission electron microscope (STEM) image was acquired using a high-angle annular dark-field (HAADF) detector. The image demonstrates how densely spaced deformation twins fragment the central grain, inter-

act with high-angle grain boundaries and are transmitted into neighboring grains. The high-resolution TEM image in Fig. 9b focuses on a region in which two deformation twins with a thickness of about 2.5 nm cross the field of observation. The fast Fourier transform (FFT) image in the inset in the upper left corner shows how the lattices of the regions denoted “1” and “2” are rotated about a common crystallographic [110] axis. The FFT image combines two sets of intensity maxima due to interference from the two twin-related regions 1 and 2. Fig. 9c represents the region outlined by a white square in Fig. 9b after additional FFT filtering. The relative orientations of the parent crystal and the twins shown in Fig. 9c can be described by the twinning elements $K_1 = (\bar{1}\bar{1}\bar{1})$, $\eta_1 = [\bar{1}12]$, $K_2 = (\bar{1}11)$, $\eta_2 = [1\bar{1}2]$ and a shear $s = 1/\sqrt{2}$, analogous to a compound fcc twin commonly reported in fcc crystals [24]. These twinning elements are indicated on the [110] projection of the atomic columns shown in Fig. 9c together with a fully indexed FFT pattern in the inset in the lower left corner. Individual indices are color-coded such that white indices correspond to the lattice in region 1 and red indices correspond to the lattice in region 2.

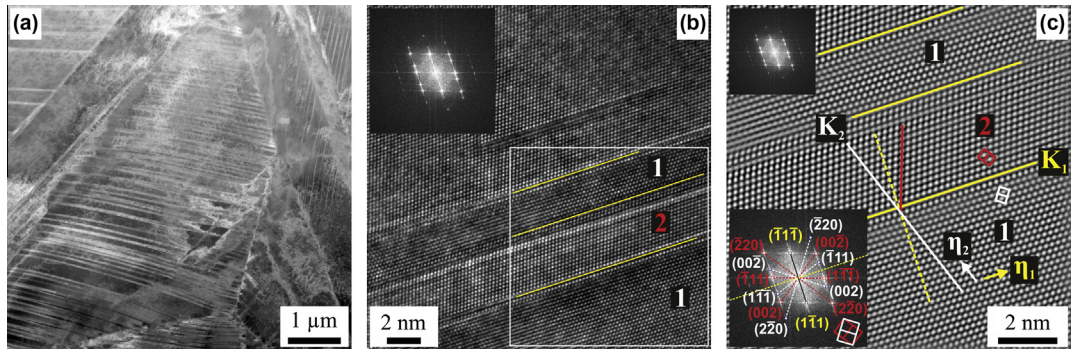


Fig. 9. TEM micrographs characterizing deformation twinning in the fine-grained CoCrFeMnNi alloy (grain size 4.4 μm) after a strain of 20.2% at 77 K. (a) Overview of the twinned microstructure acquired in the HAADF mode. (b) High-resolution TEM image of twins denoted “1” and “2”, with the corresponding FFT inset. (c) FFT-filtered image of the area outlined by the white square in (b) showing the corresponding twinning elements. The inset in the lower left corner of (c) shows the fully indexed intensity maxima in reciprocal space. (For interpretation to colors in this figure, the reader is referred to the web version of this paper.)

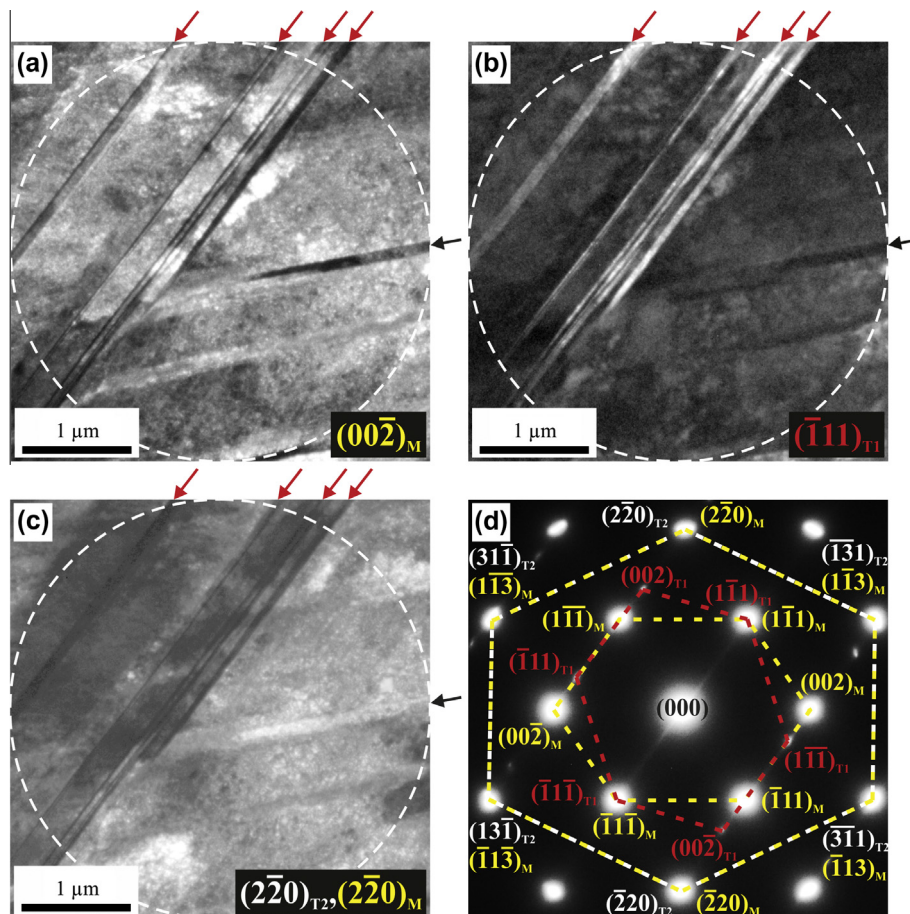


Fig. 10. Deformation twinning on more than one twinning system as observed in the coarse-grained CoCrFeMnNi alloy (grain size 155 μm) after plastic deformation of 37.8% at 77 K. The DF micrographs were formed using the beams (a) $(002)_M$, (b) $(\bar{1}11)_{T1}$ and (c) $(2\bar{2}\bar{0})_{M,T2}$. (d) The corresponding selected-area diffraction pattern, which contains the beams used to form images (a)–(c). (For interpretation to colors in this figure, the reader is referred to the web version of this paper.)

When the CG material is deformed to an even higher strain of 38.7% at 77 K, additional twinning systems are activated on {111} twinning planes that are different from the primary twinning plane. As a consequence, the deformation twins from different systems intersect each other. The three TEM dark-field (DF) images shown in Fig. 10

demonstrate this microstructural evolution. These images were acquired using the selected area diffraction (SAD) technique and are consecutively formed by electron beams passing through the $(00\bar{2})_M$, $(\bar{1}11)_T1$ and $(2\bar{2}0)_{M,T2}$ reciprocal lattice points shown in the $[110]$ -type SAD pattern of Fig. 10d. It can be clearly seen that the narrow twinned

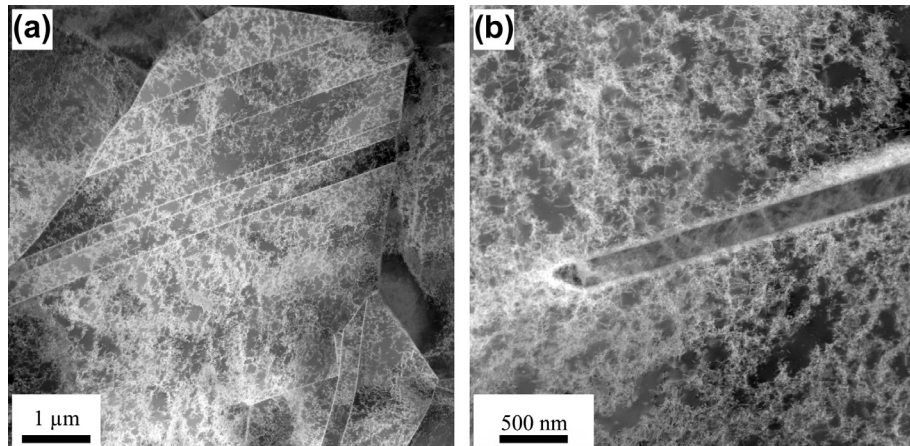


Fig. 11. Representative HAADF images showing the microstructure of the fine-grained CoCrFeMnNi alloy (grain size 4.4 μm) after plastic deformation of 20.6% at 293 K. (a) Dislocation cell structure and coarse annealing twins at low magnification. (b) Higher magnification micrograph of a different grain for the assessment of the average dislocation cell size.

regions marked by red arrows (twinning system T1) and the thicker region marked by a black arrow (twinning system T2) are dark in the image in Fig. 10a. In this case the electrons that contribute to the $(00\bar{2})_{\text{M}}$ beam are scattered mainly from the neighboring matrix, thus making the surrounding matrix appear bright. On the other hand, twins of the system T1 are bright in Fig. 10b since the corresponding $(\bar{1}11)_{\text{T}1}$ beam predominantly forms in the T1-oriented crystals. Similarly, the DF image in Fig. 10c highlights the T2 twins. Since deformation twinning has been observed in the FG (Fig. 9) and CG materials (Fig. 10) after deformation at 77 K, presumably the MG material (with intermediate grain size) also undergoes mechanical twinning at 77 K.

In contrast to what happens at 77 K, extensive deformation twinning is not observed at room temperature when samples are deformed to comparable strains. Examples are presented in Fig. 11, where two HAADF STEM images show the microstructure of the FG material after straining to 20.6% at 293 K. The overview image of Fig. 11a reveals that the dislocation structure, which was predominantly planar at low strains (see Fig. 6), has reorganized into loose dislocation cells, similar to what has been observed in other fcc alloys with low-to-medium stacking fault energy (SFE) [25]. The higher magnification micrograph in Fig. 11b shows that the cell sizes are in the range of 200–300 nm. A few twin boundaries can also be seen in both images of Fig. 11. However, based on their morphology and relatively coarse spacing, they are most probably annealing twins which were present in the grains before deformation.

4. Discussion

The results of the present study provide clear evidence that temperature and grain size influence the tensile properties of the equiatomic CoCrFeMnNi high-entropy alloy. All three of the investigated grain sizes, 4.4, 50 and 155 μm , exhibited a single-phase fcc crystal structure. A strong grain size strengthening occurred when the grain size was

decreased from 155 to 4.4 μm , with a much smaller increase for a grain size decrease from 155 to 50 μm . For each of these grain sizes, the yield and ultimate strengths increased with decreasing temperature, with the strongest increase between room temperature and liquid nitrogen temperature. Elongations to fracture also increased with decreasing temperature, although it was monotonic only for the two larger grain sizes; for the smallest grain size, there was a ductility minimum at an intermediate temperature of ~ 673 K.

Distinct yield points followed by stress drops were observed in the stress-strain curves of the FG material at temperatures of 293 and 473 K (an example is shown in the inset of Fig. 3a), but not at other temperatures and grain sizes. Ueji and co-workers [26] recently reported similar behavior for an FeMnAlSi steel: yield drops were present at a grain size of 1.8 μm but not at grain sizes of 7.2 μm or larger. It is unclear if this discontinuous yielding phenomenon is an intrinsic grain size effect or if it is merely a manifestation of dislocation pinning and breakaway from solute atmospheres or short-range order. Further research is needed to clarify this as well as the possibly related phenomenon of serrations in the stress-strain curves in the intermediate temperature range (Fig. 3) since such serrations are commonly attributed to dynamic dislocation pinning and breakaway, i.e. dynamic strain aging [27].

Dislocation slip in the initial stages of plastic deformation was found to be strongly localized (planar) within a limited set of $\{111\}$ -type slip planes as can be seen from Fig. 6. This is in line with earlier studies which investigated dislocation plasticity in concentrated binary fcc solid solutions [19,20,28,29]. Those pioneering studies suggested that the strong localization of dislocation glide on a limited number of $\{111\}$ -type planes is likely to be associated with either short-range clustering (SRC) or short-range ordering (SRO) of solute atoms. The presence of SRC and SRO gives rise to a local resistance to dislocation motion which can be interpreted in terms of a local friction stress

[19,20,28,29]. The authors argued that passage of a dislocation through a relatively ordered/clustered region on a slip plane randomizes the distribution of solute atoms and, consequently, decreases the friction stress opposing dislocation motion in that particular slip plane. This provides an easy plane for subsequent dislocations to move on and dislocation glide tends to organize into a distinct set of slip planes. Based on the experimental results presented in this study, the above scenario proposed for concentrated binary fcc solid solutions may be applicable also to the yielding region of our CoCrFeMnNi high-entropy alloy. Another possible reason for planar slip is the splitting of $1/2\langle 110 \rangle$ dislocations into $1/6\langle 112 \rangle$ Shockley partials with stacking faults in between, which would tend to minimize cross slip and confine slip to the primary $\{111\}$ planes. In support of this mechanism, numerous stacking faults were indeed observed after deformation (Fig. 7), although undissociated (full) $1/2\langle 110 \rangle$ dislocations were also observed.

The dislocation structures observed after more advanced stages of deformation (plastic strains of 20% or higher) lose their planar character as shown in Fig. 11. The transition from planar slip at low strains to loosely organized dislocation cell structures at high strains may be assisted by the following mechanism. As demonstrated in Fig. 8, dislocation multipoles form at relatively small tensile strains. These multipoles represent low-energy dislocation configurations and therefore considerably limit dislocation motion in the activated slip planes; they are thus an important contributor to dislocation hardening. When the initial slip planes are blocked by this multipole arrangement, activity on fresh slip planes is required to accommodate the externally imposed strain forcing dislocation plasticity to spread out more uniformly. A more uniform distribution of slip events results, in turn, in a more uniform destruction of SRC and/or SRO and, consequently, the friction stress in the affected material volumes. Therefore, planar slip vanishes gradually and the dislocations tend to arrange in a form that is more commonly found at low temperatures in pure fcc metals such as Cu [25].

Our study provides clear evidence that deformation twinning contributes to the accumulated strain when the CoCrFeMnNi alloy is deformed at 77 K (Figs. 9 and 10). Considering the fcc twinning shear of $s = 1/\sqrt{2}$, and assuming an average Taylor factor of $M = 3.06$ for a randomly textured material, twinning can account for a maximum strain of 23%, provided that the twinned volume is 100% of the total material; in reality, the strain that can be accommodated by deformation twinning will likely be well below this value. Despite this, the elongation to fracture increased by more than 20 percentage points (from ~50–60% to ~70–90%) when the test temperature decreased from 293 to 77 K. Therefore, there should be other reasons for the observed ductility increase, as discussed below.

When the test temperature is decreased from 293 to 77 K, a steep increase in the yield and the ultimate

strengths is observed for all three grain sizes, as shown in Fig. 4. Although both of these mechanical properties vary with temperature in a qualitatively similar way, the absolute change is more pronounced for the ultimate tensile strength due to increased work hardening at low temperatures, as illustrated in Fig. 5. This is accompanied by a transition from dislocation glide dominated plasticity at room temperature to a mixed deformation mode consisting of dislocation glide plus nanoscale twinning at 77 K. Twinning is expected to contribute to the increased work hardening at 77 K, similar to what is seen in other materials, where mechanical twinning is a major deformation mode (e.g. [30–35]). Although the exact nature and magnitude of twinning-induced strengthening is still a subject of debate in the literature, there seems to be general agreement that the formation of twins during mechanical testing results in continuous grain fragmentation by the introduction of new interfaces, which effectively reduces the dislocation mean free path and causes strengthening [34–38]. This is commonly referred to as the “dynamic Hall–Petch” effect.

The twinning-induced increase in work hardening at cryogenic temperature can postpone the formation of geometric instabilities (necking) to higher values of strain (Considere's criterion) and increase the elongation to fracture in our CoCrFeMnNi high-entropy alloy, as proposed in an earlier preliminary study [14]. This is in agreement with the conclusion drawn for other materials that undergo deformation-induced twinning and/or a martensitic transformation [39,40]. Fig. 12 illustrates this effect for the fine-grained samples that were deformed at 77, 293 and 473 K. The true stress–true strain curves in Fig. 12a were calculated from the engineering stress–engineering strain curves shown in Fig. 3a up to the point at which geometric instabilities start to form, i.e. the ultimate tensile strength. Fig. 12b plots the derivatives ($d\sigma_t/d\varepsilon_t$) of these true stress–true strain curves as a function of the true stress, σ_t . The grey area indicates the region in which necking is predicted to occur according to Considere's criterion, i.e. where $d\sigma_t/d\varepsilon_t < \sigma_t$. Two features become obvious from Fig. 12: first, for the three cases shown in the figure, the strain hardening rates are always highest at 77 K and lowest at 473 K. Second, as the test temperature is lowered, the points of intersection of the work hardening rate curves and the dashed line occur at progressively higher strain values, which predicts higher strains for the onset of necking at lower temperatures. Consistent with this, ductility increases as the temperature decreases and is highest at 77 K for all three grain sizes. Additionally, the extent of work hardening of the FG material is slightly, but systematically, lower than that of the MG and CG materials (Fig. 5), and its ductility is consequently lower (Fig. 4d).

The temperature at which the deformation mechanism changes (e.g. from dislocation glide at 293 K to glide plus twinning at 77 K) has been shown previously to depend on various factors such as the chemical composition or strain rate [24], and changes in the SFE [30,33]. In fcc

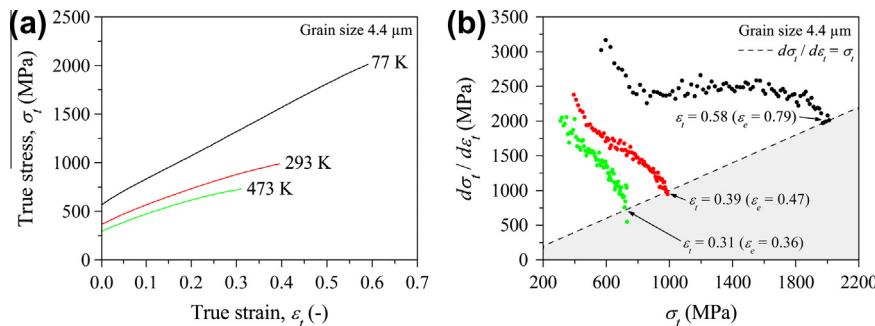


Fig. 12. (a) True stress–true strain curves calculated from the engineering stress–engineering strain curves (Fig. 3a) up to the point at which geometric instabilities start to form, i.e. the ultimate tensile strength. (b) Work hardening rate (derivative of the true stress–true strain curves, $d\sigma_t/d\varepsilon_t$) plotted as a function of the true stress, σ_t , for fine-grained samples (grain size 4.4 μm) deformed at 77 K (black symbols), 293 K (red symbols) and 473 K (green symbols). The grey area (underneath the dashed line) is where geometric instability (necking) is expected according to Considere's criterion, i.e. where the work hardening rate is less than the true stress. (For interpretation to colors in this figure, the reader is referred to the web version of this paper.)

alloys, low-to-medium SFEs (\sim 18–45 mJ m^{-2}) favor the formation of deformation twins [41], while an fcc \rightarrow hexagonal close-packed phase transformation can be observed when the SFE is even lower [42]. A rationale for this behavior is that both of these low SFE deformation processes are related to the dissociation of perfect dislocations into Shockley partials and thus to the formation of a stacking fault in between these partials. Idrissi et al. [43] recently provided convincing microstructural evidence for the role of intrinsic and extrinsic stacking faults as precursors for the formation of deformation-induced twins and ε -martensite, respectively, in an interstitial-free FeMnAlSi alloy. Hence, if the SFE increases with temperature, the propensity for twinning or deformation-induced phase transformations may be expected to decrease as well.

Unfortunately, for the CoCrFeMnNi high-entropy alloy investigated here, neither the SFE nor its temperature dependence is known. The microstructural evidence presented in Fig. 7, however, demonstrate that SFs can be found after deformation over the whole temperature range investigated. Moreover, no obvious change in the deformed microstructures is observed as a function of temperature after low plastic strains of about 2%, as shown in Fig. 6, where planar slip is identified to be the main deformation mechanism before the onset of twinning. Planar slip is expected in low SFE materials [44] since the dissociation of dislocations makes cross slip more difficult. Therefore, neither observation supports the idea that a drastic increase in SFE with temperature is the main reason for why twinning disappears as a deformation mode at room temperature and above in the CoCrFeMnNi alloy. Instead, it seems more plausible that this transition is related to the pronounced temperature dependence of the yield strength (Figs. 3 and 4). The data in Fig. 4c show that the ultimate tensile strength of the FG material (grain size, 4.4 μm) is around 660 MPa at 293 K. When the test temperature is decreased to 77 K, this stress is reached at a plastic strain of less than 5%. A detailed investigation of the twinning stress for the CoCrFeMnNi alloy has yet to be conducted, but Fig. 6 clearly shows that a certain degree of dislocation

plasticity precedes the onset of twinning since no deformation twins were observed at strains less than 2.4% at 77 K. It is therefore conceivable that the stress that is needed to induce deformation by twinning cannot be reached when specimens are deformed at room temperature even if other intrinsic material properties such as the SFE remained approximately constant.

The strong temperature dependence of the yield stress observed in the present high-entropy alloy between 77 and 293 K is not typically seen in pure fcc metals. As shown in Fig. 4a, the absolute differences in the yield strength between 77 and 293 K are almost independent of grain size, with values of 205, 194 and 185 MPa for the FG, MG and CG materials, respectively. The $\sigma_y(T)$ curves for materials of different grain sizes are roughly parallel up to intermediate temperatures (873 K). As a consequence, it can be inferred that the temperature dependence of the yield stress at low temperatures (below 873 K) is not influenced significantly by grain size. A refinement of the grain size causes merely a vertical shift of the yield stress vs. temperature curves in Fig. 4a. For each of these curves, the temperature-dependent yield strength, $\sigma_y(T)$, can be viewed as the sum of thermal and athermal components [44,45]:

$$\sigma_y(T) = \sigma_{\text{th}} + \sigma_{\text{ath}}, \quad (1)$$

where σ_{th} and σ_{ath} are the thermal and athermal contributions, respectively. Unlike in body-centered cubic metals, where the Peierls stress is significant, in pure fcc metals σ_{th} is usually negligible, resulting in a temperature-independent yield strength [46]. However, it can be significant in some binary fcc solid solutions; most such studies have been performed on alloys where Cu is the solvent [47–53]. In binary Cu–Al, Cu–Ge or Cu–Mn solid solution alloys, it has been shown that σ_{th} increases with increasing solute content [45,47]. Furthermore, the critical temperature (T_c) at which the yield strength transitions from being temperature-dependent to being temperature-independent shifts to higher temperatures with increasing solute concentrations. In dilute solutions, the energy barriers to dislocation motion, since they can be overcome by thermal activation at

relatively low temperatures, must be short-range obstacles on the order of a Burgers vector [49]. The obstacles in more concentrated solid solutions, like the present high-entropy alloy, must be stronger since they require greater thermal activation to overcome. The nature of these obstacles, especially in equiatomic high-entropy alloys where there are multiple principal elements and, therefore, no “solute” or “solvent”, is an interesting topic for further study. Even the nature of a dislocation line, which is normally viewed as being made up of mostly the same kind of atom, needs re-evaluation in the case of a high-entropy solid solution alloy that consists of multiple principal elements.

5. Summary and conclusions

An equiatomic CoCrFeMnNi high-entropy alloy was produced by arc melting, drop casting and rolling, after which it was recrystallized to produce single-phase, fcc-structured, equiaxed microstructures with three different grain sizes, 4.4, 50 and 155 μm. The temperature and grain size dependencies of its tensile properties were investigated in the temperature range 77–1073 K. To interpret the mechanical properties, microstructural analyses were performed by TEM before and after deformation. Based on our observations, the following conclusions can be drawn.

- (1) Up to test temperatures of 873 K, yield strength increased with decreasing grain size, with the greatest increase occurring when the grain size was decreased from 155 to 4.4 μm and only a modest increase occurring when it was decreased from 155 to 50 μm. Ultimate tensile strength also increased with decreasing grain size, though to a lesser extent than yield strength. Elongation to fracture was comparable for the two coarser grain sizes and lower for the finer grain size material.
- (2) For all three grain sizes, the alloy shows a strong increase in yield and ultimate tensile strengths with decreasing temperature. Elongation to fracture also increased with decreasing temperature, monotonically for the two coarser grains, but with an intermediate temperature minimum at around 673 K for the fine-grained material.
- (3) In the temperature range of 77–873 K, initial plasticity, up to tensile strains of about 2%, occurs exclusively by planar glide of $1/2\langle 110 \rangle$ dislocations on {111} planes. Stacking faults were observed consistent with splitting of these dislocations into $1/6\langle 112 \rangle$ Shockley partials. Planar slip could be the result of the first dislocations to move on a slip plane, destroying short-range order or clustering and making it easier for the following dislocations to move on the same slip plane. Stacking-fault-coupled partial dislocations could be another reason for planar slip by making cross slip harder. At higher strains, at room temperature and above, slip became more homogeneous and cell structures developed.

- (4) Upon lowering the test temperature from room temperature to 77 K, nanoscale twinning was observed as an additional deformation mode in specimens interrupted after strains of 20% or more, but not in specimens interrupted shortly after yielding (strains around 2%). This deformation-induced twinning, by providing an additional deformation mode, likely contributes to the observed increase in ductility at low temperatures. Additionally, twinning introduces extra interfaces within the grains during deformation (“dynamic Hall–Petch”); therefore, it increases the work hardening rate and the ultimate tensile strength. This increase in work hardening postpones the onset of necking instability to higher strains (Considere’s criterion) and is another reason for the higher ductility at 77 K compared to that at room temperature.
- (5) The increase in yield strength with decreasing temperature seen in this fcc high-entropy alloy is not typically observed in pure fcc metals. However, it is known to occur in *binary* fcc solid solutions to varying degrees, depending on the solute concentration. Our TEM analyses to date have not provided an explanation for this temperature dependence of yield strength. Further studies are needed to shed light on the thermally activated microstructural processes that govern yielding in equiatomic high-entropy solid solution alloys in which the terms “solute” and “solvent” lose their conventional meanings.

Acknowledgements

This research was supported by the US Department of Energy, Basic Energy Sciences, Materials Sciences and Engineering Division. F.O. also received funding from the Alexander von Humboldt Foundation through a Feodor Lynen Research Fellowship. A.D. received financial support through the IPM AS CR development program no. RVO:68081723.

References

- [1] Yeh JW, Chen SK, Lin SJ, Gan JY, Chin TS, Shun TT, et al. *Adv Eng Mater* 2004;6:299.
- [2] Cantor B, Audebert F, Galano M, Kim KB, Stone IC, Warren PJ. *J Metastable Nanocryst Mater* 2005;24–25:1.
- [3] Cantor B. *Ann Chim Sci Mater* 2007;32:245.
- [4] Munitz A, Kaufman MJ, Chandler JP, Kalaantari H, Abbaschian R. *Mater Sci Eng A* 2013;560:633.
- [5] Ng C, Guo S, Luan J, Shi S, Liu CT. *Intermetallics* 2012;31:165.
- [6] Liu L, Zhu JB, Zhang C, Li JC, Jiang Q. *Mater Sci Eng A* 2012;548:64.
- [7] Tong CJ, Chen MR, Chen SK, Yeh JW, Shun TT, Lin SJ, et al. *Metall Mater Trans A* 2005;36:1263.
- [8] Wang XF, Zhang Y, Qiao Y, Chen GL. *Intermetallics* 2007;15:357.
- [9] Zhou YJ, Zhang Y, Wang YL, Chen GL. *Mater Sci Eng A* 2007;454–455:260.
- [10] Zhu JM, Fu HM, Zhang HF, Wang AM, Li H, Hu ZQ. *Mater Sci Eng A* 2010;527:6975.

- [11] Senkov ON, Wilks GB, Scott JM, Miracle DB. *Intermetallics* 2011;19:698.
- [12] Senkov ON, Scott JM, Senkova SV, Miracle DB, Woodward CF. *J Alloys Compd* 2011;2011:6043.
- [13] Liu WH, Wu Y, He JY, Nieh TG, Lu ZP. *Scripta Mater* 2013;68:526.
- [14] Gali A, George EP. *Intermetallics* 2013;39:74.
- [15] Cantor B, Chang ITH, Knight P, Vincent AJB. *Mater Sci Eng A* 2004;375–377:213.
- [16] Otto F, Yang Y, Bei H, George EP. *Acta Mater* 2013;61:2628.
- [17] Loebel R. In: Weast RC, editor. *Handbook of chemistry and physics*. Cleveland (OH): CRC Press; 1974.
- [18] Dlouhy A, Eggeler G. *Pract Metallogr* 1996;33:629.
- [19] Gerold V, Kärnthal HP. *Acta Metall* 1989;37:2177.
- [20] Neuhäuser H. *Acta Metall* 1975;23:455.
- [21] Korner A, Kärnthal HP. *Phys Status Solidi* 1981;21:19.
- [22] Hirsch P, Howie A, Nicholson RB, Pashley DW, Whelan MJ. *Electron microscopy of thin crystals*. Washington (DC): Butterworths; 1965.
- [23] Williams DB, Carter CB. *Transmission electron microscopy Part 3: Imaging*. 2nd ed. New York: Springer; 2009.
- [24] Christian JW, Mahajan S. *Prog Mater Sci* 1995;39:1.
- [25] Landau P, Shneck RZ, Makov G, Venkert A. *MRS Proc* 2006;982:0982-KK09-05.
- [26] Ueji R, Tsuchida N, Terada D, Tsuji N, Tanaka Y, Takemura A, et al. *Scripta Mater* 2008;59:963.
- [27] Robinson JM, Shaw MP. *Int Mater Rev* 1994;39:113.
- [28] Olfe J, Neuhäuser H. *Phys Status Solidi A* 1988;109:149.
- [29] Blessing J, Achmus Ch, Neuhäuser H, Schönfeld B, Kostorz G. *Z Metallkd* 1997;88:630.
- [30] Rémy L, Pineau A. *Mater Sci Eng* 1976;26:123.
- [31] Rémy L. *Acta Metall* 1978;26:443.
- [32] Asgari S, El-Danaf E, Kalidindi R, Doherty R. *Metall Mater Trans A* 1997;28:1781.
- [33] Rohatgi A, Vecchio KS, Gray GT. *Metall Mater Trans A* 2001;32:135.
- [34] Beladi H, Timokhina IB, Estrin Y, Kim J, De Cooman BC, Kim SK. *Acta Mater* 2011;59:7787.
- [35] Gutierrez-Urrutia I, Raabe D. *Acta Mater* 2011;59:6449.
- [36] Raghavan RS, Sastri AS, Marcinkowski MJ. *Trans AIME* 1969;245:1569.
- [37] Karaman I, Sehitoglu H, Beaudoin AJ, Chumlyakov YI, Maier HJ, Tomé CN. *Acta Mater* 2000;48:2031.
- [38] Bouaziz O, Guelton N. *Mater Sci Eng A* 2001;319–321:246.
- [39] Garde AM, Aigeltinger E, Reed-Hill RE. *Metall Trans* 1973;4:2461.
- [40] Grässel O, Krüger L, Frommeyer G, Meyer LW. *Int J Plast* 2000;16:1391.
- [41] Curtze S, Kuokkala VT. *Acta Mater* 2010;58:5129.
- [42] Frommeyer G, Brüx U, Neumann P. *ISIJ Int* 2003;43:438.
- [43] Idrissi H, Ryelandt L, Veron M, Schryvers D, Jacques PJ. *Scripta Mater* 2009;60:941.
- [44] Hong SI, Laird C. *Acta Metall Mater* 1990;38:1581.
- [45] Schwink Ch, Wille Th. *Scr Metall* 1980;14:1093.
- [46] Cottrell AH. *The mechanical properties of matter*. New York: Wiley; 1964.
- [47] Koppenaal TJ, Fine ME. *Trans AIME* 1962;224:347.
- [48] Mitchell TE. In: Stanford EG, Fearon JH, McGonnagle WJ, editors. *Progress in applied materials research*, vol. 6. London: Heywood; 1964.
- [49] Wigley DA. *Mechanical properties of materials at low temperatures*. New York: Plenum Press; 1971.
- [50] Basinski ZS, Foxall RA, Pascual R. *Scripta Metall* 1972;6:807.
- [51] Traub H, Neuhäuser H, Schwink Ch. *Acta Metall* 1977;25:437.
- [52] Wille Th, Schwink Ch. *Acta Metall* 1986;6:1059.
- [53] Butt MZ, Aziz F, Ali D. *J Alloys Compd* 2010;498:102.